Nano Research

Open Access

Research Article

# An ionic liquid assisted *in-situ* growth of large-area and high-crystal-quality perovskite single-crystal thin films

Min Liao[1,§], Zhaojin Wang[1,§], Chengwei Shan[1,§], Dengfeng Luo[1,2], Zhongyuan Guan[1], Qingqian Wang[1,4], Hongmei Zhu[1], Zhulu Song[1], Dan Wu[3] ✉, Aung Ko Ko Kyaw[1] ✉, and Kai Wang[1] ✉

[1] *Department of Electronic and Electrical Engineering, Southern University of Science and Technology, Shenzhen 518055, China*
[2] *Peng Cheng Laboratory, Shenzhen 518055, China*
[3] *College of New Materials and New Energies, Shenzhen Technology University, Shenzhen 518118, China*
[4] *Institute of Physics, Henan Academy of Sciences, Zhengzhou 450046, China*
[§] *Min Liao, Zhaojin Wang, and Chengwei Shan contributed equally to this work.*

**Cite this article:** *Nano Research*, **2025**, *18*, 94907046. https://doi.org/10.26599/NR.2025.94907046

**ABSTRACT:** *In-situ* growth of perovskite single-crystal thin films (PeSCTFs) on the transport layer is crucial for achieving high-performance perovskite optoelectronic devices, such as solar cells, light emitting diodes, photodetectors, etc. However, *in-situ* growing PeSCTF on the transport layer with large-area, high-crystal-quality, and low-trap-density simultaneously remains challenging. This work proposes a method for *in-situ* growing large-area and low-trap-density $MAPbBr_3$ SCTFs on the poly[bis(4-phenyl)(2,4,6-trimethylphenyl)amine] (PTAA) transport layer with the assistance of cesium(I) bis(trifluoromethanesulfonyl)imide (CsTFSI) ionic liquid. After introducing the CsTFSI ionic liquid, the $Cs^+$ ions enter the $MAPbBr_3$ lattice, reducing the formation energy, and the coordination between the lone pair electrons of O in $TFSI^-$ and the empty orbital of Pb in $MAPbBr_3$ passivates the dangling bond defects of Pb, facilitating the formation of $MAPbBr_3$ SCTFs with high-crystal-quality. Moreover, the strong interaction between $TFSI^-$ and the substrate can enhance wettability and reduce the contact angle, thereby promoting faster solute diffusion and enabling the growth of larger-area $MAPbBr_3$ SCTFs. Therefore, compared to the sample without CsTFSI addition, the $MAPbBr_3$ SCTFs with CsTFSI addition exhibit better thermal stability, larger area (increased from 1.79 to 19.68 $mm^2$, approximately a 10-fold increase), lower trap density (decreased from $6.86 \times 10^{12}$ to $5.39 \times 10^{12}$ $cm^{-3}$), and higher carrier mobility (increased from 0.72 to 0.84 $cm^2 \cdot V^{-1} \cdot s^{-1}$). Moreover, the performance of the photodetector with CsTFSI, including responsivity, external quantum efficiency (EQE), detectivity, and response speed, also increased significantly. This work provides an effective method for the *in-situ* growth of PeSCTFs with large-area, high-crystal-quality, and low-trap-density simultaneously on the transport layer.

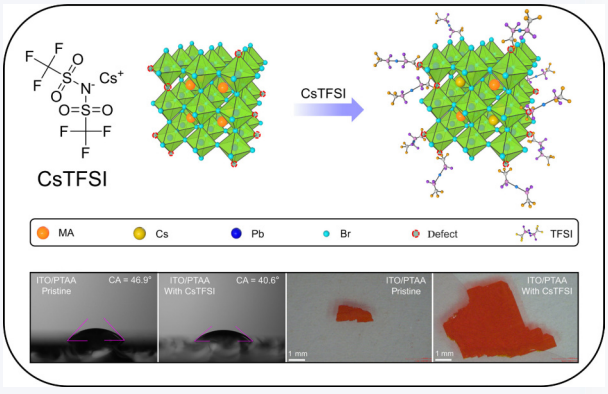


**KEYWORDS:** perovskite single-crystal thin films, ionic liquid, *in-situ* growth, photodetector

## 1 Introduction

Organic–inorganic metal halide perovskites have been deeply investigated for applications in solar cells [1], light-emitting diodes (LEDs) [2], photodetectors [3], lasers [4], and so on [5]. In the field of photodetectors, they exhibit excellent properties such as high light absorption coefficients, high carrier mobility, tunable bandgaps, and low cost [6–8]. In perovskite thin films, compared to polycrystalline films, perovskite single-crystal thin films (PeSCTFs) have fewer grain boundaries or even no grain boundaries, which is beneficial for the fabrication of high-performance optoelectronic devices with low trap state density [9–12]. Moreover, PeSCTFs exhibit enhanced characteristics such as extended carrier diffusion length, prolonged carrier lifetime, increased carrier mobility, and heightened stability, thereby facilitating the further enhancement of efficiency and stability in optoelectronic devices [13–18].

Currently, PeSCTFs can be grown on a variety of substrates, such as silicon, graphene, indium tin oxide (ITO), fluoro-doped tin oxide

**Received:** July 15, 2024; **Revised:** September 17, 2024
**Accepted:** September 23, 2024

✉Address correspondence to Dan Wu, wudan@sztu.edu.cn; Aung Ko Ko Kyaw, aung@sustech.edu.cn; Kai Wang, wangk@sustech.edu.cn

(FTO), polyimide (PI), polyethylene (PE), polyethylene terephthalate (PET), $SrTiO_3$, $MoS_2$, quartz, and solution substrates [19–27]. However, PeSCTFs grown on these substrates cannot be directly applied to vertically structured optoelectronic devices because the active layer (PeSCTFs) of hybrid perovskite-based high-performance solar cells, LEDs, and photodetectors is usually sandwiched between the electron transport layer (ETL) and the hole transport layer (HTL) [28, 29]. Therefore, PeSCTFs grown on these substrates require an additional stripping and transfer process to the transport layer, which can lead to the formation of new defects and mechanical damage on the surface of the PeSCTFs [30]. *In-situ* growth of PeSCTFs on the transport layer can eliminate the need for this additional stripping process, thereby reducing interface contact issues between the PeSCTFs and the transport layer [31, 32]. The methods for preparing PeSCTFs mainly include chemical vapor deposition method [33], top to down method [34], floating method [35], epitaxial growth method [36], anti-solvent method [24], and spatial confinement method [37]. Among these methods, the spatial confinement method is compatible with many single-crystal preparation methods and is cost-effective, allowing for *in-situ* growth on the transport layer [35, 38, 39]. It is widely known that growing large-area PeSCTFs (van der Waals epitaxy) *in-situ* at the transport layer requires the crystals to grow parallel to the layer-island. Layer-island growth necessitates a strong interaction between the precursor solution and the substrate, which indicates good wettability, i.e., a larger interfacial energy. If the interfacial energy is too small, it leads to island-like growth instead of layer-island growth, resulting in small-area single-crystal films distributed in an island-like pattern [40]. Unfortunately, there are currently two undesirable situations in the preparation of PeSCTFs using spatial confinement method. If PeSCTFs prepared by spatial confinement method have a larger area, their crystal quality is generally poorer, prone to dendrite formation. This is because the contact angle between the perovskite precursor solution and the transport layer is small, resulting in high interfacial energy and fast nucleation and diffusion rates for PeSCTFs. Conversely, if the crystal quality of PeSCTFs prepared by spatial confinement method is good, it is due to a large contact angle, low interfacial energy, slow nucleation rate, and slow diffusion rate, which may lead to a smaller area for PeSCTFs [41–43]. Therefore, producing PeSCTFs with large-area and high-crystal-quality using spatial confinement methods remains a challenge.

In 2017, Huang et al. developed a spatial confinement method combined with high-temperature methods for the *in-situ* growth of $MAPbI_3$ and $MAPbBr_3$ SCTFs on the hole transport layer. In 2018, Liu and Zhao et al. reported the preparation of $PEA_2PbI_4$ SCTFs using a spatial confinement method combined with gradient cooling. In 2019, Osman M. Bakr et al. developed a spatial confinement method combined with gradient heating for the *in-situ* growth of $MAPbI_3$ SCTFs on the hole transport layer. In 2022 and 2023, our research group systematically studied the kinetics of crystal nucleation and growth by the spatial confinement method and proposed a method for the *in-situ* growth of PeSCTFs on the transport layer using a spatial confinement method combined with gradient heating nucleation and room temperature growth (GHN-RTG) [41, 44]. However, this method is insufficient to resolve the contradiction in the growth of existing PeSCTFs, which still cannot grow PeSCTFs with both large-area and high-crystal-quality.

The primary challenges in achieving large-area and high-crystal-quality growth of $MAPbBr_3$ materials stem from the relatively high formation energy of $MAPbBr_3$ and the larger contact angle between the solution and the substrate. In this work, we propose adding cesium(I) bis(trifluoromethanesulfonyl)imide (CsTFSI) ionic liquid to assist in the *in-situ* growth of large-area and high-crystal-quality $MAPbBr_3$ PeSCTFs. By introducing CsTFSI ionic liquid, the $Cs^+$ cations can enter the $MAPbBr_3$ lattice to reduce the formation energy of $MAPbBr_3$. This also enhances the interaction between the solution and the substrate, thereby reducing the contact angle. The surface area of the obtained $MAPbBr_3$ SCTFs increased by approximately 10 times. A series of material characterizations demonstrated that adding CsTFSI ionic liquid led to higher crystal quality, lower trap density, and improved thermal stability in $MAPbBr_3$ SCTFs. Furthermore, the photodetector showed increased responsivity, higher external quantum efficiency, and higher detectivity after adding CsTFSI ionic liquid. Additionally, the response speed was also improved. This work provides a new approach for *in-situ* growth of large-area, high-crystal quality, and low-trap density PeSCTFs on the transport layer.

## 2 Results and discussion

### 2.1 Material characterization of $MAPbBr_3$ SCTFs

Using the GHN-RTG method to grow $MAPbBr_3$ SCTFs *in-situ* on the poly[bis(4-phenyl)(2,4,6-trimethylphenyl)amine] (PTAA) HTL, but this method cannot simultaneously produce large-area and high-quality crystal PeSCTFs [44]. Based on this, the method of using CsTFSI ionic liquid to assist *in-situ* growth of PeSCTFs was adopted. After introducing CsTFSI ionic liquid, the contact angle of the precursor solution on the PTAA substrate was reduced from 46.9° to 40.6°, as shown in Figs. 1(a) and 1(b). The contact angle reflects the cohesion and adhesion of the solution to the substrate. The decrease in contact angle while the solution remains unchanged, and the cohesive forces of solution molecules remain constant, indicates an increase in the adhesive forces between the solution and the substrate [45]. This indicates that introducing CsTFSI ionic liquid can enhance the interaction between $MAPbBr_3$ SCTFs and substrate, leading to a faster diffusion rate of the solute. On the other hand, as the contact angle becomes smaller, the interfacial energy becomes larger, and the nuclear barrier of the crystal decreases. As the crystal nucleation rate increases, the crystal growth rate will also increase, indicating that CsTFSI ionic liquid can accelerate the crystal nucleation and growth of SCTFs.

Figures 1(c) and 1(d) represent photographs of $MAPbBr_3$ SCTFs without and with the addition of CsTFSI, respectively, at the same time after complete growth. The photographs reveal that after the introduction of CsTFSI, the area of $MAPbBr_3$ SCTFs increased from 1.79 to 19.68 $mm^2$, approximately by a factor of 10. The thicknesses of the two films are 25 and 24 μm, respectively. The area-thickness ratios reach 71.6 and 820 mm, respectively, before and after the addition of CsTFSI. This indicates that the introduction of CsTFSI can enlarge the area of $MAPbBr_3$ SCTFs. Figures S1(a) and S1(b) in the Electronic Supplementary Material (ESM) present step profilometer tests at six different positions (illustrated schematically in the lower right corner of the figure) on $MAPbBr_3$ SCTFs. It can be observed that the surface fluctuations do not exceed 40 nm, indicating that the $MAPbBr_3$ SCTF surface is very flat. The surface roughness measurements for a large area of 400 $\mu m^2$ of $MAPbBr_3$ SCTFs are shown in Figs. S1(c) and S1(d) in the ESM, with an average roughness of about 1.6 nm, similarly indicating that the $MAPbBr_3$ SCTFs are comparatively flat. The composition of $MAPbBr_3$ SCTFs with and without the addition of

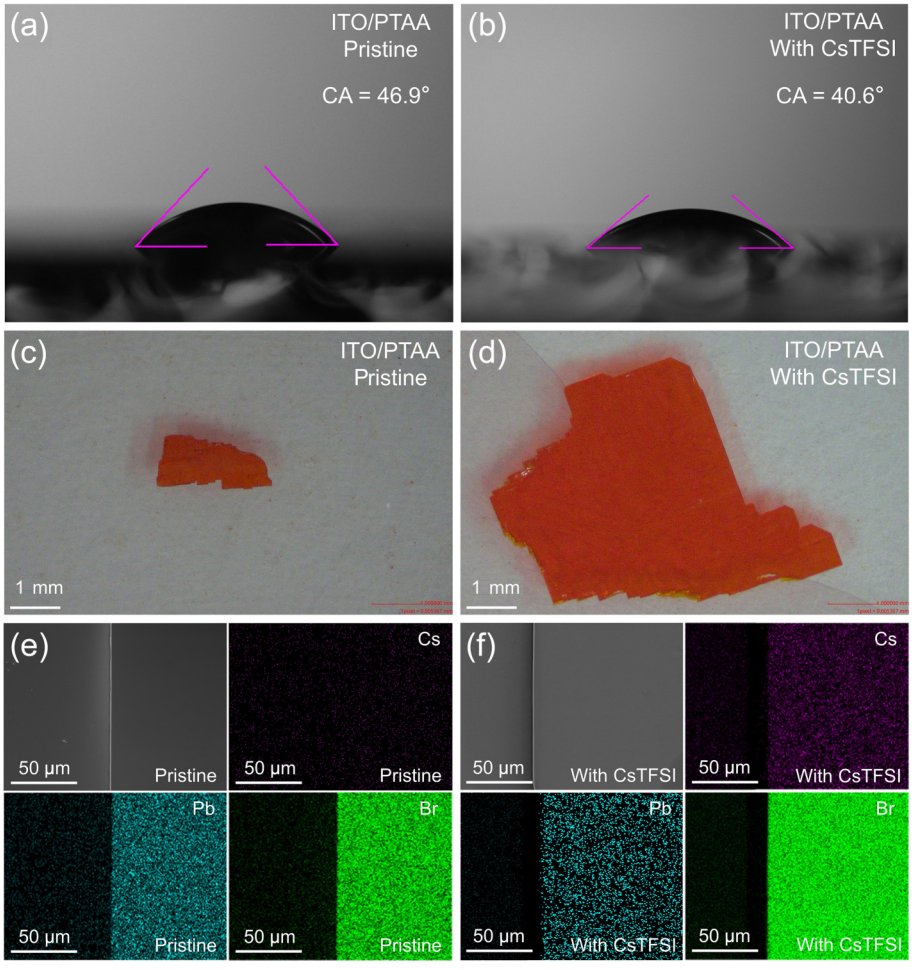


**Figure 1** Contact angle optical photograph of (a) precursor solution and (b) precursor solution with CsTFSI ionic liquid added on ITO substrate spun with PTAA. Microscopic images of (c) $MAPbBr_3$ SCTFs and (d) $MAPbBr_3$ SCTFs with CsTFSI. The SEM and EDS mapping analysis of Cs, Pb, and Br for (e) $MAPbBr_3$ SCTFs and (f) $MAPbBr_3$ SCTFs with CsTFSI.

CsTFSI can be determined through the energy dispersive X-ray spectrometer (EDS) mapping analysis, as shown in Figs. 1(e) and 1(f), with the respective elemental ratios given in Table S1 in the ESM. It can be observed that $Cs^+$ ions from CsTFSI have entered the lattice of $MAPbBr_3$.

To investigate the internal quality changes of $MAPbBr_3$-SCTFs before and after the introduction of CsTFSI, we conducted the X-ray diffraction (XRD) characterization and the results are shown in Figs. 2(a) and 2(b). Both $MAPbBr_3$ SCTFs exhibit high single crystallinity with three characteristic peaks with centers located at 14.90°, 30.09°, and 45.87°, corresponding to the (100), (200), and (300) planes of cubic $MAPbBr_3$ crystals, respectively. After the introduction of CsTFSI, the XRD peak of $MAPbBr_3$ SCTFs significantly increased, and the full width half maximum (FWHM) of the (200) crystal plane also significantly decreased. This indicates that the crystal quality of $MAPbBr_3$ SCTFs is improved after the introduction of CsTFSI. Meanwhile, the diffraction peak at 30.09° on the right side of Fig. 2(a) indicates a shift towards larger angles after adding CsTFSI, suggesting a reduction in the unit cell volume. This further indicates that introducing CsTFSI results in smaller $Cs^+$ ions entering the $MAPbBr_3$ lattice to replace the larger methylammonium ions ($MA^+$). This can reduce the local strain gradient caused by the larger organic cation insertion and thereby suppress phase segregation [46]. To illustrate the universality of CsTFSI ionic liquids, $MAPbCl_3$ SCTFs and $MAPbI_3$ SCTFs were treated similarly, as shown in Fig. S2 in the ESM. It can be concluded that after adding CsTFSI ionic liquid, the XRD diffraction peaks of $MAPbCl_3$ SCTFs and $MAPbI_3$ SCTFs are significantly enhanced, indicating that CsTFSI ionic liquid can also improve the crystal quality of $MAPbCl_3$ SCTFs and $MAPbI_3$ SCTFs. Therefore, the CsTFSI ionic liquid has certain versatility in aiding the growth of PeSCTFs.

The trap density of thin film samples can be analyzed by fluorescence intensity and lifetime. In the case of the same material system and dimension, the higher the fluorescence intensity, the longer the fluorescence lifetime, and the lower the trap density of the corresponding thin film [47]. After introducing CsTFSI, the fluorescence intensity of $MAPbBr_3$ SCTFs was enhanced by more than 8 times, and the fluorescence lifetime was also increased by 4 times. As shown in Figs. 2(c)–2(e), introducing CsTFSI can reduce the trap density of $MAPbBr_3$ SCTFs. It can be observed from the photoluminescence (PL) spectrum that there is a blue shift phenomenon. However, the slight thickness variations of $MAPbBr_3$ SCTFs have a negligible effect on the blue shift of the PL spectrum, as shown in Fig. S3 in the ESM. Therefore, the blue shift of the PL peak is mainly due to the $Cs^+$ in the CsTFSI ionic liquid entering the $MAPbBr_3$ lattice, which increases the bandgap. The absorption spectra are shown in Fig. 2(f), and the absorption peak also presents

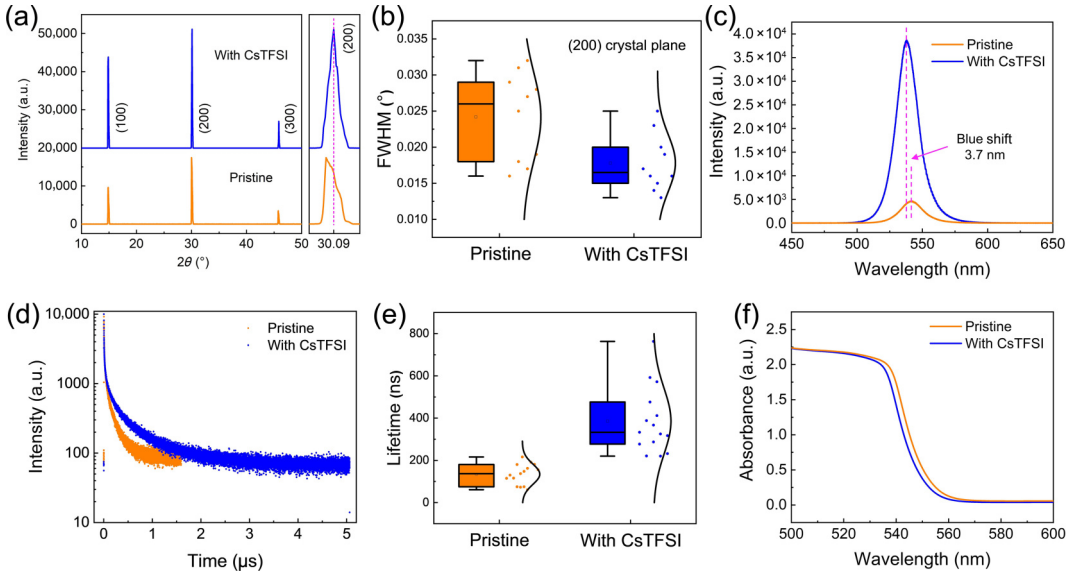


**Figure 2** (a) XRD patterns, (b) FWHM of the (200) crystal plane, (c) PL, (d) time-resolved PL (TRPL) decay curves, (e) lifetime, and (f) absorption spectra of $MAPbBr_3$ SCTFs without and with CsTFSI.

a slight blue shift, which is consistent with the PL. By Tauc fitting of the absorption spectra (Fig. S4(a) in the ESM), the bandgap of $MAPbBr_3$ SCTFs without CsTFSI ionic liquid was determined to be 2.26 eV. The bandgap of $MAPbBr_3$ SCTFs with CsTFSI ionic liquid added was 2.27 eV. The introduction of CsTFSI ionic liquid resulted in an increase of 0.01 eV in the bandgap. It is further demonstrated that adding CsTFSI ionic liquid makes $Cs^+$ enter the $MAPbBr_3$ lattice to increase the bandgap.

*In-situ* temperature-dependent XRD analysis was employed to assess the thermal stability of the SCTFs. Figures 3(a) and 3(b) present *in-situ* temperature-dependent XRD patterns of $MAPbBr_3$ SCTFs grown with and without CsTFSI. At the same temperature, the intensity of the diffraction peak is higher, indicating that the introduction of CsTFSI ionic liquid improves the quality of the crystal. In *in-situ* heating process, $MAPbBr_3$ SCTFs without CsTFSI ionic liquid began to decompose at 160 °C, resulting in the $PbBr_2$ phase. However, $MAPbBr_3$ SCTFs with CsTFSI ionic liquid did not decompose until 200 °C, indicating that the addition of ionic liquid can significantly improve the thermal stability of SCTFs. The increase of thermal stability is mainly due to the decrease of trap density and $Cs^+$ entering the lattice.

The lattice strain of SCTFs was characterized by Raman spectroscopy (Fig. 3(c)). In Raman spectroscopy, a higher intensity of the Raman peak indicates a lower trap density [36]. It can be clearly seen from Fig. 3(c) that 63 $cm^{-1}$ belongs to $[PbBr_6]^{4-}$ stretching vibration [44], 141 $cm^{-1}$ belongs to Pb–Br stretching [36], 327 $cm^{-1}$ belongs to $CH_3NH_3^+$–$PbBr_3^-$ cage vibration [48], and 969 $cm^{-1}$ belongs to C–$N^+$ stretching [48]. The results showed that all tensile vibrations of $MAPbBr_3$ SCTFs with CsTFSI were significantly higher than those of $MAPbBr_3$ SCTFs. Therefore, $MAPbBr_3$ SCTFs with the addition of CsTFSI exhibit less trap density. The hardness of SCTFs was characterized by the nanoindentation meter, as shown in Fig. 3(d). Material hardness is usually determined by the interaction of atoms or ions. The higher

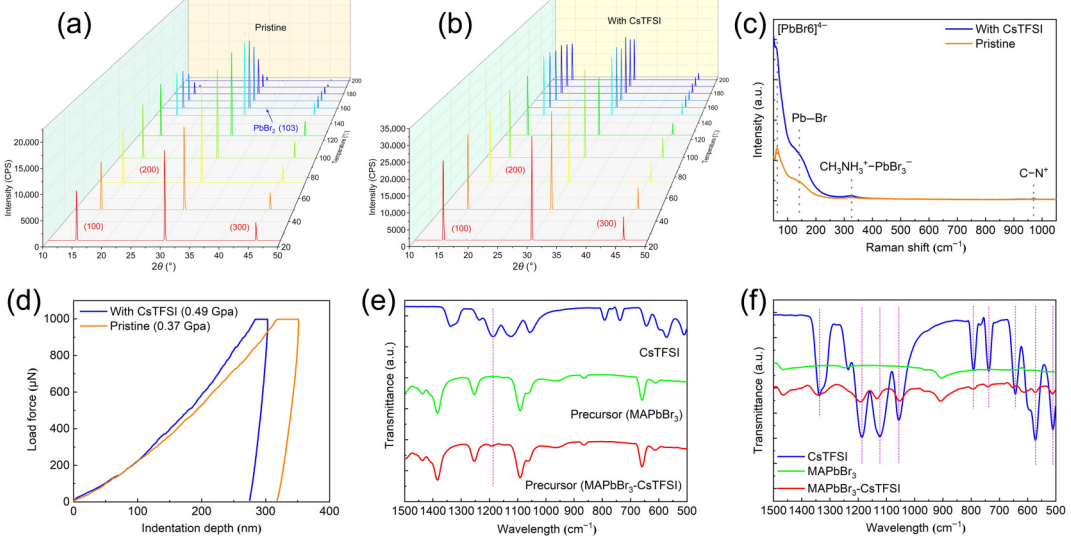


**Figure 3** The temperature-dependent XRD tests of (a) $MAPbBr_3$ SCTFs and (b) $MAPbBr_3$ SCTFs with CsTFSI. (c) Raman spectroscopy and (d) pressure and depth curves of $MAPbBr_3$ SCTFs without and with CsTFSI. The FTIR of (e) precursor and (f) $MAPbBr_3$ SCTFs without and with CsTFSI.

the crystal quality, the stronger the interaction, the greater the hardness, and the smaller the deformation with pressure [49]. After the introduction of CsTFSI, the hardness of $MAPbBr_3$ SCTFs increased from 0.37 to 0.49 GPa, an increase of 32%. This is because CsTFSI reduces the defect state density of $MAPbBr_3$ SCTFs, resulting in improved crystal quality. In addition, the thickness, surface roughness performed in a 1 $\mu m^2$ area, and surface conductivity of $MAPbBr_3$ SCTFs were characterized (Figs. S4(b) and S5 in the ESM). It can be seen that the surface of $MAPbBr_3$ SCTFs after the introduction of CsTFSI is smooth and flat with high electrical conductivity, indicating fewer surface defects.

The surface chemical information of $MAPbBr_3$ SCTFs was characterized using Fourier transform infrared (FTIR) spectroscopy. The main FTIR characteristic peaks of CsTFSI are 511, 573, 644, 737, 793, 1057, 1126, 1188, and 1337 $cm^{-1}$ (Figs. 3(e) and 3(f)). The FTIR spectra of CsTFSI, precursor solution without and with CsTFSI are shown in Fig. 3(e). The presence of CsTFSI in the precursor solution of $MAPbBr_3$-CsTFSI can be observed from the pink line. When the CsTFSI ionic liquid is present in the precursor solution, it does not participate in the binding of $PbBr_2$ and does not compete with N,N-dimethylformamide (DMF) for crystallization, indicating that the interaction between $TFSI^-$ and $PbBr_2$ is not as strong as DMF and $PbBr_2$. From the pink line in Fig. 3(f), it can be seen that there is a significant absorption peak of CsTFSI in the $MAPbBr_3$ SCTFs after adding CsTFSI. Furthermore, a blue shift is observed in the same absorption peak, indicating a strong coordination interaction between $TFSI^-$ and $Pb^{2+}$, which passivates the dangling bond defects of Pb. Therefore, the dangling bond defects of Pb can be effectively passivated after the introduction of CsTFSI ionic liquid, thus effectively reducing the defect state density of SCTFs.

The surface chemical information of $MAPbBr_3$ SCTFs was characterized by X-ray photoelectron spectroscopy (XPS) [50]. As shown in Figs. 4(a)–4(c), it can be seen that the $MAPbBr_3$ SCTFs with CsTFSI added have the XPS characteristic peaks of Cs $3d_{3/2}$, Cs $3d_{5/2}$, S 2p, and F 1s, while the $MAPbBr_3$ SCTFs without CsTFSI added do not have these characteristic peaks. This shows that $Cs^+$ and $TFSI^-$ exist in the $MAPbBr_3$ SCTF, consistent with the previous discussion. Ultraviolet photoelectron spectroscopy (UPS) is often used to analyze the carrier transport characteristics of perovskite films. UPS was used to characterize the energy level position on the surface of $MAPbBr_3$ SCTFs, as shown in Figs. 4(d) and 4(e). From the graph, it can be seen that after the addition of CsTFSI ionic liquid, the Fermi level increased from −5.14 to −5.02 eV, and the energy distance between the Fermi level and the valence band increased from 0.80 to 0.82 eV. Based on the previously fitted bandgap values, the introduction of CsTFSI ionic liquid caused the valence band of $MAPbBr_3$ SCTFs to shift from −5.94 to −5.84 eV. As shown in Fig. 4(f), moving the energy level upwards will make the valence band maximum more matched with the energy level of the HTL (PTAA). This will accelerate the extraction and separation of charge carriers, and improve the transport of charge carriers on the surface of the thin film [3, 51]. The primary reason for the upward shift in energy levels is that $TFSI^-$ forms a relatively strong coordination effect with $Pb^{2+}$, which passivates the dangling bond defects of Pb, resulting in a reduction in the defect state density of $MAPbBr_3$ SCTFs. Here, it is believed that CsTFSI reduces the defect state density of $MAPbBr_3$ SCTFs because $TFSI^-$ forms a strong

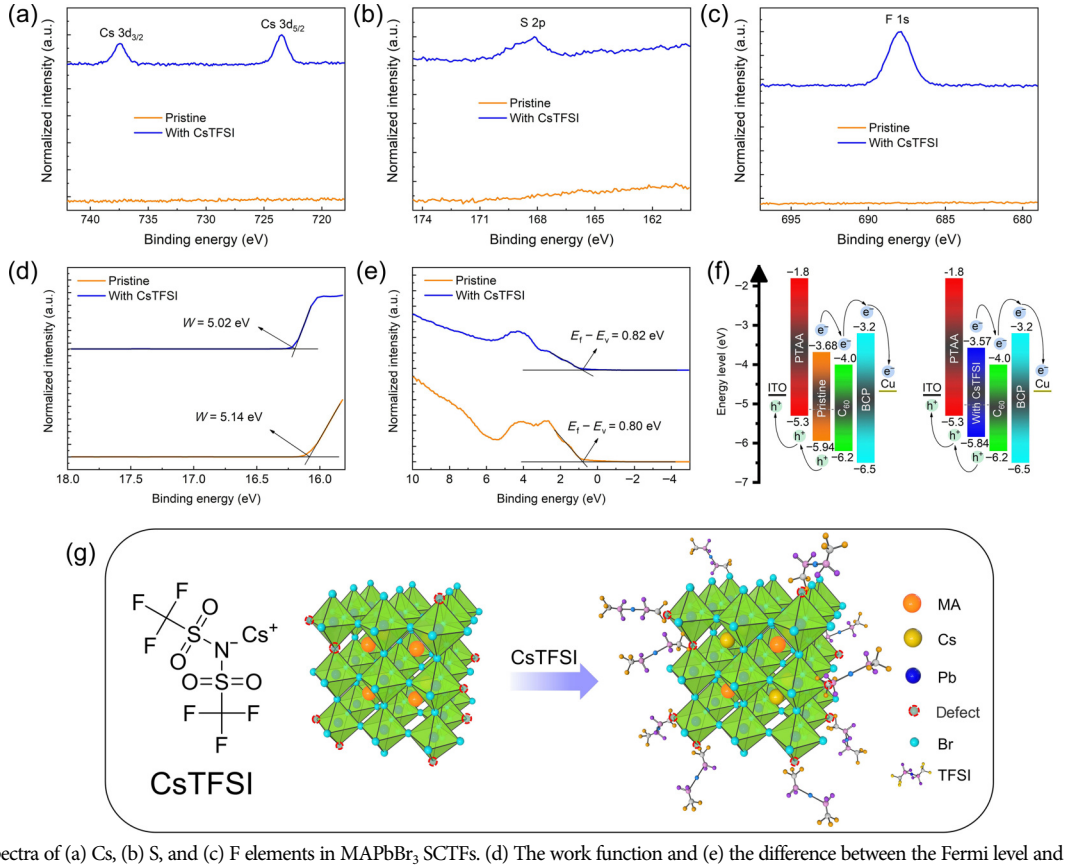


**Figure 4** XPS spectra of (a) Cs, (b) S, and (c) F elements in $MAPbBr_3$ SCTFs. (d) The work function and (e) the difference between the Fermi level and the valence band of $MAPbBr_3$ SCTFs without and with CsTFSI. (f) Energy level diagram of ITO, PTAA, $MAPbBr_3$, $C_{60}$, BCP, and Cu. (g) The structural formula of CsTFSI ionic liquid and the crystal structure diagram of $MAPbBr_3$ before and after adding CsTFSI.

coordination effect with $Pb^{2+}$, which passivates the dangling bond defects of Pb. According to the first principles calculation, the binding energy between Pb and F is −0.434 eV, and between Pb and O is −1.234 eV (Fig. S6 in the ESM). It can be seen that the binding energy of Pb and O is higher, so the addition of CsTFSI ionic liquid to $MAPbBr_3$ SCTFs is the lone pair electron of O and the empty orbital coordination of Pb.

The structure of CsTFSI is shown on the left side of Fig. 4(g). As shown on the right of Fig. 4(g), $Cs^+$ cations enter the $MAPbBr_3$ lattice after adding CsTFSI to reduce the formation energy [52, 53]. $TFSI^-$ anion can passivate the surface defects of $MAPbBr_3$, which is conducive to forming $MAPbBr_3$ SCTFs [54, 55]. To verify that both $Cs^+$ cations and $TFSI^-$ anions in CsTFSI ionic liquids played an essential role in the growth of $MAPbBr_3$ SCTFs, a comparative experiment was conducted to compare the growth of $MAPbBr_3$ SCTFs after adding $Cs_2CO_3$, LiTFSI, and CsTFSI, respectively. For the $Cs_2CO_3$, although the dissociated $Cs^+$ can enter the lattice of $MAPbBr_3$, reducing the formation energy and facilitating the rapid growth of SCTFs, the $CO_3^{2-}$ do not effectively enhance the interaction between $MAPbBr_3$ and the substrate. As shown in Fig. S7(a) in the ESM, the contact angle difference between with $Cs_2CO_3$ and without addition is not significant. Therefore, merely reducing the formation energy without increasing wettability can result in excessive growth leading to dendritic formation, rather than forming larger areas of SCTFs. The use of LiTFSi as a comparison is because it contains the $TFSi^-$ anion. This anion has a high electronegativity and can effectively passivate the $Pb^{2+}$ dangling bond defects on the surface of the perovskite [54, 55]. In addition, the S and O atoms in $TFSi^-$ can form hydrogen bonds with the H atoms in PTAA, and the N atoms in $TFSI^-$ can also form hydrogen bonds with the H atoms in PTAA. The stronger interaction between the precursor solution and the substrate can increase wettability and reduce the contact angle (Fig. S7(b) in the ESM). However, since $Li^+$ cannot enter the lattice and thus cannot reduce the formation energy, the increased wettability leads to excessive growth, which ultimately also easily forms dendrites. For CsTFSi, on one hand, the $Cs^+$ entering the lattice lowers the formation energy, favoring the formation of $MAPbBr_3$ SCTFs. On the other hand, $TFSI^-$ facilitates enhanced interaction between the solution and the substrate, thereby reducing the contact angle. The lower formation energy facilitates the rapid formation of the $MAPbBr_3$ phase, while the smaller contact angle benefits the solute transport during the growth process of $MAPbBr_3$. The synergistic effect of both facilitates the rapid growth of large-area $MAPbBr_3$ SCTFs. As shown in Fig. S7(c) in the ESM, $MAPbBr_3$ SCTFs grown after adding CsTFSI have a larger surface area, while those grown after adding $Cs_2CO_3$ or LiTFSI have a smaller surface area. This indicates that the combined action of $Cs^+$ cation and $TFSI^-$ anion in CsTFSI ionic liquid increases the area of $MAPbBr_3$ SCTFs, which is consistent with the previous analysis.

## 2.2 Electrical properties of $MAPbBr_3$ SCTFs

The defect state density can be characterized by the space charge-limited current (SCLC) method, and the device structure is ITO/PTAA/perovskite/Au (area 0.25 $mm^2$ and film thickness 24 μm), as shown in Figs. 5(a) and 5(b). This dark state *I*–*V* curve can be divided into three regions, namely, the ohmic region (light purple), the trap-filling region (SCLC region, light green), and the saturation region (light pink). The turning point voltage in the ohmic region and SCLC region is called the trap filling voltage, and the equation for calculating the defect state density ($n_{trap}$) according to the filling voltage is shown as follows (Eq. (1)) [17]

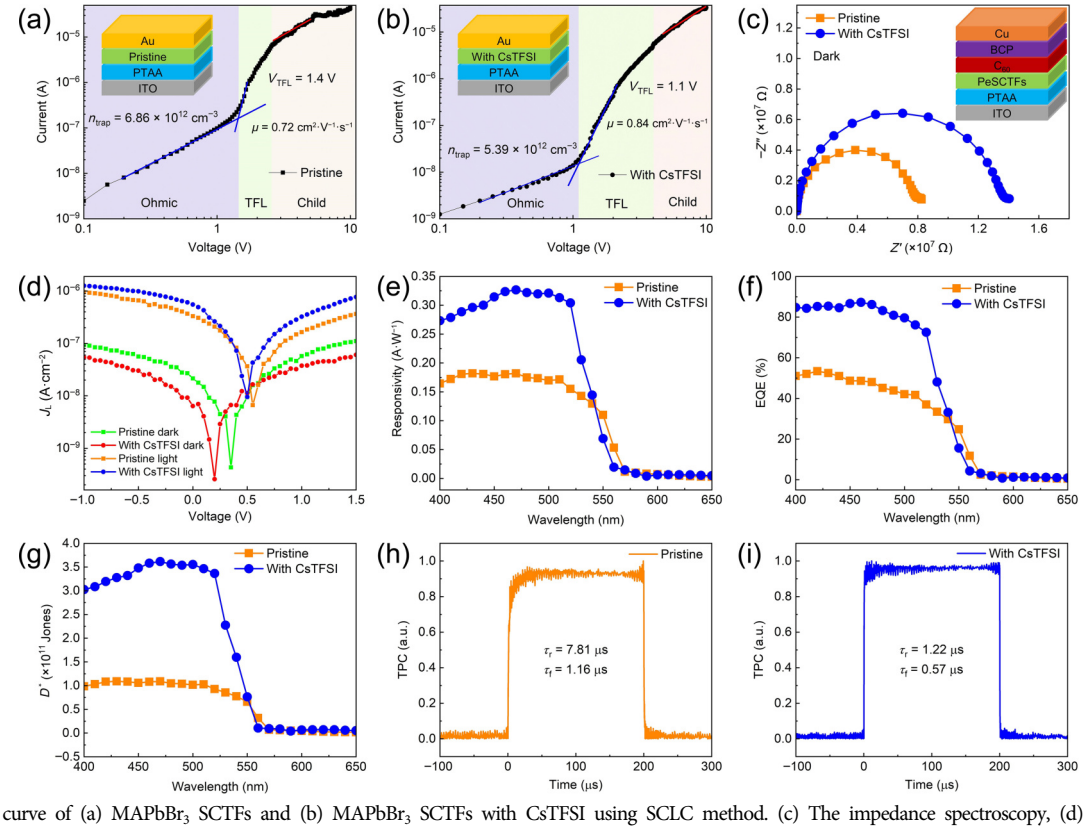


**Figure 5** *I*–*V* curve of (a) $MAPbBr_3$ SCTFs and (b) $MAPbBr_3$ SCTFs with CsTFSI using SCLC method. (c) The impedance spectroscopy, (d) *J*–*V* curves, (e) responsivity, (f) EQE, (g) detectivity, and (h) and (i) response time of the photodetector.

$$n_{trap} = 2\varepsilon\varepsilon_0 V_{TFL}/qL^2 \quad (1)$$

where $q$ is the fundamental charge, $\varepsilon$ is the relative dielectric constant of $MAPbBr_3$ single crystal ($\varepsilon$ = 25.5), $\varepsilon_0$ is the vacuum dielectric constant, $V_{TFL}$ is the trap filling voltage, and $L$ is the thickness of the $MAPbBr_3$ SCTF. The trap filling voltage ($V_{TFL}$) of the single crystal film decreased from 1.4 to 1.1 V after introducing CsTFSI ionic liquid. According to Eq. (1), the introduction of CsTFSI ionic liquid reduces the $MAPbBr_3$ SCTF defect state density from $6.86 \times 10^{12}$ to $5.39 \times 10^{12}$ $cm^{-3}$, reducing by 21%, as shown in Figs. 5(a) and 5(b). The reduction in defect state density confirms the strong coordination effect between $TFSI^-$ and $Pb^{2+}$, which passivates the dangling bond defects of Pb.

According to the Mott–Gurney law [56], the carrier mobility for the $MAPbBr_3$ single crystal in the trap-free region was further calculated (Eq. (2)) [17]

$$\mu = 8J_D L^3/9\varepsilon\varepsilon_0 V^2 \quad (2)$$

where $J_D$ is the dark current density, $V$ is the applied bias, and $\mu$ is the carrier mobility. As shown in Figs. 5(a) and 5(b), the device structure is a hole-only device, so the calculated carrier mobility is the hole mobility. According to Eq. (2), the introduction of CsTFSI ionic liquid increases the carrier (hole) mobility of $MAPbBr_3$ SCTFs from 0.72 to 0.84 $cm^2 \cdot V^{-1} \cdot s^{-1}$, an increase of 17%. The increase in carrier mobility indicates the reduction in defect state density of $MAPbBr_3$ SCTFs, leading to an upward shift in energy level position. This, in turn, improves energy level matching and enhances carrier separation and extraction efficiency.

Due to the lower defect state density and higher carrier mobility of $MAPbBr_3$ SCTFs after the addition of CsTFSI, subsequent characterization of the photodetector made from $MAPbBr_3$ SCTFs was conducted. A self-driven photodetector (ITO/PTAA/PeSCTFs/$C_{60}$/BCP/Cu) was prepared by using $MAPbBr_3$ SCTFs with a thickness of 24 μm grown on PTAA substrate, and the diagram of the device structure is shown in the upper right corner of Fig. 5(c). The trap density of $MAPbBr_3$ SCTFs can be characterized by electrochemical impedance spectroscopy, as shown in Fig. 5(c). The large semicircle obtained from the Nyquist plot corresponds to the radiative recombination process of charge carriers at the interface [57]. The large semicircular circle in the Nyquist diagram corresponds to the recombination resistance of $MAPbBr_3$ SCTFs with CsTFSI ionic liquid added, which is 14 MΩ (14,046,200 Ω). This is much larger than the recombination resistance of the original $MAPbBr_3$ SCTFs 8 MΩ (8,255,210 Ω). The larger recombination resistance indicates a lower trap density and less interface radiative recombination, which is beneficial for enhancing the separation of charge carriers and improving the performance of optoelectronic devices such as solar cells and photodetectors [58].

The current density and voltage characteristic curve of the detector are shown in Fig. 5(d). Under dark conditions, the voltage corresponding to the lowest dark current is not close to 0 V. This is because the crystal growth is unstable, and the surface of SCTFs prepared by solution methods often contains small crystal particles, leading to charge accumulation at the interface caused by the poor contact between the SCTF and the $C_{60}$ ETL [38, 44, 59–61]. The minimum dark current density of the photodetector with added CsTFSI is closer to zero than that of the original photodetector. In addition, the minimum dark current density of the photodetector with added CsTFSI ($2.6 \times 10^{-10}$ $A \cdot cm^{-2}$) is lower than that of the original photodetector ($4.3 \times 10^{-10}$ $A \cdot cm^{-2}$). Meanwhile, the ratio of the photocurrent density to the dark current density for the photodetector with added CsTFSI (37.1) is greater than that of the original photodetector (15.4). This is because the $MAPbBr_3$ SCTFs with added CsTFSI ionic liquid have a higher crystal quality and lower defect state density.

Responsivity, external quantum efficiency (EQE), and specific detectivity are parameters used to characterize the photoelectric conversion capability of photodetectors. The responsivity is the ratio of the photocurrent to the incident light intensity, representing the efficiency of responding to optical signals. The EQE is the number of carriers generated in the external circuit for each incident photon. The specific detectivity represents the ability to detect weakest level of light [61]. The responsivity ($R(\lambda)$) was calculated as follows (Eq. (3)) [59, 60, 62, 63]

$$R(\lambda) = (I(\lambda)_{ph} - I_{dark})/P(\lambda)_{in} \quad (3)$$

where $I(\lambda)_{ph}$ is the photocurrent, $I_{dark}$ is the dark current, and $P(\lambda)_{in}$ refers to the light power irradiated to the device.

The equation for calculating EQE($\lambda$) according to $R(\lambda)$ is as follows (Eq. (4)) [59, 60, 62, 63]

$$EQE(\lambda) = R(\lambda)hc/q\lambda \quad (4)$$

where $h$ is the Plank constant, $c$ is the speed of light in vacuum, and $\lambda$ is the detection wavelength.

The equation for calculating specific detectivity ($D^*$) according to $R(\lambda)$ is as follows (Eq. (5)) [59, 60, 62, 63]

$$D^* = R(\lambda)(Area/I_n^2)^{1/2} \approx R(\lambda)(Area/2qI_{dark})^{1/2} \quad (5)$$

where Area refers to the working area of the photodetector, in square centimeters, and $I_n$ refers to the total noise current spectral density. The total noise current in a photodetector is the sum of various noises, which can be approximated in practical calculations. The responsivity ($R(\lambda)$), EQE, and specific detectivity ($D^*$) of the self-driven photodiode at 0 V bias and light intensity of 2.7 $\mu W \cdot cm^{-2}$ are shown in Figs. 5(e)–5(g), respectively. Adding CsTFSI, the responsivity of the photodetector (0.33 $A \cdot W^{-1}$) is higher than the original photodetector (0.18 $A \cdot W^{-1}$), increased by 83%. The EQE (87.3%) is higher than the original photodetector (53.4%), increased by 63%. Additionally, the detectivity of the photodetector after adding CsTFSI ($3.61 \times 10^{11}$ Jones) is higher than the detectivity of the original photodetector ($1.09 \times 10^{11}$ Jones), increased by 231%. This is due to the fact that the photodetector after the addition of CsTFSI ionic liquid shows a lower trap density (Figs. 5(a) and 5(b)) and a larger interfacial recombination resistance (Fig. 5(c)), which facilitates the acceleration of carrier separation. The responsivity, EQE, and specific detectivity of the wavelength curve are similar to the absorption spectra of SCTF. These are caused by the wavelength-dependent Abs coefficients of the $MAPbBr_3$ material and are reflected in the responsivity, EQE, and $D^*$ curves of the photodetector.

Response speed is also another quality factor parameter of photodetectors, which is important for optical communication and imaging applications. The rise time ($\tau_r$) is the time it takes for the current to reach a 90% stable level under light, while the fall time ($\tau_f$) is defined as the time it takes to fall to the 10% saturation level after the light source is turned off. As shown in Figs. 5(h) and 5(i), the response speed of the photodetector after adding CsTFSI ($\tau_r$ = 1.22 μs; $\tau_f$ = 0.57 μs) is faster than that of the original photodetector

($\tau_r$ = 7.81 μs, $\tau_f$ = 1.16 μs). This is due to higher carrier mobility and lower carrier migration trap density. Therefore, the data in Fig. 5 show that the photodetector with CsTFSI ionic liquid added is superior to the photodetector without CsTFSI ionic liquid added.

## 3 Conclusions

Large-area, high-crystal-quality, and low trap density $MAPbBr_3$ SCTFs were grown on the PTAA transport layer by employing the CsTFSI ionic liquid-assisted GHN-RTG method. The $Cs^+$ in CsTFSI ionic liquid reduces the formation energy after entering the $MAPbBr_3$ lattice. The coordination between the lone pair electrons of O in $TFSI^-$ and the empty orbital of Pb in $MAPbBr_3$ passivates the dangling bond defects of Pb, thereby filling the lattice defects of $MAPbBr_3$, favoring the formation of $MAPbBr_3$ SCTFs. Moreover, the stronger interaction between $TFSI^-$ and the substrate can enhance wettability and reduce the contact angle, thereby promoting faster solute diffusion, which is the reason for obtaining large-area $MAPbBr_3$ SCTFs. XRD characterization indicates that the addition of CsTFSI ionic liquid results in $MAPbBr_3$ with higher crystal quality. Temperature-dependent XRD characterization suggests that the inclusion of CsTFSI ionic liquid can significantly enhance the thermal stability of SCTFs. Material characterizations including PL, TRPL, Raman spectroscopy, nanoindentation, FTIR, UPS, and others demonstrate that $MAPbBr_3$ obtained after the addition of CsTFSI ionic liquid exhibits lower trap density. Furthermore, photodetectors obtained after adding CsTFSI ionic liquid have lower trap density and higher carrier mobility. At the same time, the responsivity, EQE, $D^*$, and response speed are improved. This work has guiding significance for *in-situ* growth of PeSCTFs with large-area, high-crystal-quality, and low trap density.

## 4 Experimental

### 4.1 Materials

Methylammonium bromide (MABr, 99.9%), methylammonium iodide (MAI, 99.9%) and methylamine hydrochloride (MACl, 99.9%) were purchased from Great Cell. Lead bromide ($PbBr_2$, 99.99%), lead iodide ($PbI_2$, 99.99%), lead chloride ($PbCl_2$, 99.99%), and CsTFSI (98%) were bought from TCI. DMF (99.8%) and chlorobenzene (CB, 99.5%) were purchased from Sigma-Aldrich. PTAA (99.9%), bathocuproine (BCP, 99.9%), and fullerene ($C_{60}$, 99.99%) were bought from Xi'an Polymer Light Technology. All reagents were directly used after purchase without further purification.

### 4.2 *In-situ* growth and device fabrication of PeSCTFs

ITO glass with the size of 50 mm × 50 mm was ultrasonic cleaned with ITO cleaning solution, anhydrous ethanol, and deionized water for 20 min, respectively, and dried with oxygen plasma for 5 min to improve the surface energy of ITO. Then, the PTAA solution (2 mg·mL$^{-1}$ in CB) was spin-coated on the surface of ITO at 3000 rpm for 45 s and annealed at 120 °C for 20 min to form ITO/PTAA film.

MAX (MAX is methylammonium halide, X = Cl, Br, and I) and $PbX_2$ were dissolved in DMF with a concentration of 0.4 mmol·mL$^{-1}$ at the ratio of 1.2:1, in which 0.01 g·mL$^{-1}$ CsTFSI ionic liquid was added to the experimental sample. The precursor solution was formed by stirring vigorously for 24 h and filtered by 0.22 μm filter element. The precursor solution (60 μL) was dropped on the ITO/PTAA film covered glass substrate, and another ITO/PTAA film covered glass substrate was pressed on it to form a sandwich structure. The heating procedure of the crystal nucleation stage was set as follows. The first stage was heated from 30 to 60 °C within 60 h, then held for 20 h. The second stage heating rised from 60 °C to high temperature at a heating rate of 1 °C·h$^{-1}$ (high temperature: 90 °C for $MAPbBr_3$, 80 °C for $MAPbCl_3$, and 100 °C for $MAPbI_3$). In the third stage, the heating was kept at a high temperature for 40 h, then it was cooled to room temperature for 30 days to obtain PeSCTFs.

The SCLC device was a sandwich structure of ITO/PTAA/PeSCTFs/Au, a thickness of SCTFs of 24 μm. The Au was vacuum evaporated on ITO/PTAA/PeSCTFs with 100 nm (0.5 Å·s$^{-1}$) thickness. The device structure of the photodetector was ITO/PTAA/PeSCTFs/$C_{60}$/BCP/Cu. The $C_{60}$, BCP and Cu were vacuum evaporated on ITO/PTAA/PeSCTFs with 20 nm (0.1 Å·s$^{-1}$), 8 nm (0.02 Å·s$^{-1}$), and 145 nm (0.5 Å·s$^{-1}$) thickness, respectively.

### 4.3 Characterization

A contact angle meter (JC200C1, Powereach, China) was used to measure the contact angle. A field-emission scanning electron microscopy (SEM) (Gemini SEM 300) was used to acquire the morphology inspection. The corresponding mapping analyses were identified using an EDS attached to the SEM. An X-ray diffractometer (Rigaku Smartlab) equipped with Cu K$\alpha$1 radiation ($\lambda$ = 1.54056 Å) and K$\alpha$2 radiation ($\lambda$ = 1.54439 Å) was utilized to collect the XRD and temperature-dependent XRD data. Laser confocal Raman spectroscopy (LabRAM HR Evolution) was used to characterize the PL and Raman spectra of SCTFs, with the laser excitation wavelengths of 325 and 785 nm, respectively. A fluorescence lifetime spectrometer (PicoQuant Fluotime300) under a 405-nm laser pulse was used to acquire the TRPL data. An ultraviolet–visible near-infrared spectrometer (Lambda 750 s) was utilized to collect the absorption spectra data. The step profiler obtained the thickness data (Dektalk XT, Bruker). Atomic force microscopy (AFM) (MFP-3D-Stand Alone, Asylum Research) was employed to characterize the surface roughness and conductivity of SCTFs. The nanoindentation apparatus (Hysitron TI950) characterized the hardness of SCTFs. The FTIR (Bruker Vertex 70v) was employed to characterize the surface chemical information of SCTFs. The surface chemical information of SCTFs was further characterized by XPS (Thermo ESCALAB 250XI). The UPS (Thermo ESCALAB 250XI) was used to characterize the position of energy level on the SCTF surface. The semiconductor parametric instrument (Keithley 4200A-SCS) characterized the electrical properties and detector performance of SCTFs.

### 4.4 Computational methods

Density functional theory (DFT) calculations with Perdew–Burke–Ernzerhof exchange-correlation functional were performed to understand the binding of the $MAPbBr_3$ crystal surfaces with ionic liquid (CsTFSI), using the Vienna *ab initio* simulation package [64–67]. They were treated as valence electrons, and their interactions were described by the projected augmented wave (PAW) approach [68]. A slab model was built to calculate the surface adsorption of CsTFSI on a $MAPbBr_3$ crystal surface, the $MAPbBr_3$ (100) surface was cleaved with a 20 Å vacuum layer. The binding energies ($E_b$) of CsTFSI with $MAPbBr_3$ surface were calculated as $E_{mol/pvsk} - E_{pvsk} - E_{mol}$, where $E_{mol/pvsk}$, $E_{pvsk}$, and $E_{mol}$ are the total energies of the adsorption system, the $MAPbBr_3$ surface

system, and CsTFSI, respectively. The K points considered about the symmetry of the crystal structures were used to sample the Brillouin zone, and the cutoff energy of the plane-wave basis was set to 400 eV.

**Electronic Supplementary Material**: Supplementary material (XRD, absorption spectrum, thickness, surface roughness and conductivity, growth photos, etc.) is available in the online version of this article at https://doi.org/10.26599/NR.2025.94907046.

## Data availability

All data needed to support the conclusions in the paper are presented in the manuscript and the Electronic Supplementary Material. Additional data related to this paper may be requested from the corresponding author upon request.

## Acknowledgements

This research was funded by the National Natural Science Foundation of China (Nos. 62122034 and 62405085), the Postdoctoral Fellowship Program of China Postdoctoral Science Foundation (No. GZC20231048), the Guangdong Basic and Applied Basic Research Foundation (Nos. 2022A1515011071 and 2024A1515010773), Natural Science Foundation of Top Talent of Shenzhen Technology University (SZTU) (No. GDRC202110), and Shenzhen Stable Support Research Foundation (No. 20220717215521001). We also thank the test support from the shiyanjia lab (www.shiyanjia.com).

## Declaration of competing interest

All the contributing authors report no conflict of interests in this work.

## Author contribution statement

M. L.: Conceptualization, data curation, formal analysis, investigation, software, writing – original draft, writing – review & editing. Z. J. W.: Conceptualization, data curation, formal analysis, investigation, software, writing – original draft, writing – review & editing. C. W. S.: Conceptualization, data curation, formal analysis, investigation, software, methodology, writing – original draft. D. F. L.: Methodology, software, validation. Z. Y. G.: Validation, visualization. Q. Q. W.: Funding acquisition, validation. H. M. Z.: Validation, visualization. Z. L. S.: Validation, visualization. D. W.: Funding acquisition, project administration, resources, supervision, writing – original draft, writing – review & editing. A. K. K. K.: Funding acquisition, project administration, resources, supervision. K. W.: Funding acquisition, project administration, resources, supervision, writing – original draft, writing – review & editing. All the authors have approved the final manuscript.

## Use of AI statement

None.

## References

[1] Burschka, J.; Pellet, N.; Moon, S. J.; Humphry-Baker, R.; Gao, P.; Nazeeruddin, M. K.; Grätzel, M. Sequential deposition as a route to high-performance perovskite-sensitized solar cells. *Nature* **2013**, *499*, 316–319.

[2] Lin, K. B.; Xing, J.; Quan, L. N.; de Arquer, F. P. G.; Gong, X. W.; Lu, J. X.; Xie, L. Q.; Zhao, W. J.; Zhang, D.; Yan, C. Z. et al. Perovskite light-emitting diodes with external quantum efficiency exceeding 20 per cent. *Nature* **2018**, *562*, 245–248.

[3] García de Arquer, F. P.; Armin, A.; Meredith, P.; Sargent, E. H. Solution-processed semiconductors for next-generation photodetectors. *Nat. Rev. Mater.* **2017**, *2*, 16100.

[4] Zhu, H. M.; Fu, Y. P.; Meng, F.; Wu, X. X.; Gong, Z. Z.; Ding, Q.; Gustafsson, M. V.; Trinh, M. T.; Jin, S.; Zhu, X. Y. Lead halide perovskite nanowire lasers with low lasing thresholds and high quality factors. *Nat. Mater.* **2015**, *14*, 636–642.

[5] Zhang, L. X.; Mei, L. Y.; Wang, K. Y.; Lv, Y. H.; Zhang, S.; Lian, Y. X.; Liu, X. K.; Ma, Z. W.; Xiao, G. J.; Liu, Q. et al. Advances in the application of perovskite materials. *Nano-Micro Lett.* **2023**, *15*, 177.

[6] Sutherland, B. R.; Sargent, E. H. Perovskite photonic sources. *Nat. Photonics* **2016**, *10*, 295–302.

[7] Kovalenko, M. V.; Protesescu, L.; Bodnarchuk, M. I. Properties and potential optoelectronic applications of lead halide perovskite nanocrystals. *Science* **2017**, *358*, 745–750.

[8] Li, C. L.; Ma, Y.; Xiao, Y. F.; Shen, L.; Ding, L. M. Advances in perovskite photodetectors. *Infomat* **2020**, *2*, 1247–1256.

[9] Rong, Y. G.; Hu, Y.; Mei, A. Y.; Tan, H. R.; Saidaminov, M. I.; Seok, S. I.; McGehee, M. D.; Sargent, E. H.; Han, H. W. Challenges for commercializing perovskite solar cells. *Science* **2018**, *361*, eaat8235.

[10] Dong, Q. F.; Fang, Y. J.; Shao, Y. C.; Mulligan, P.; Qiu, J.; Cao, L.; Huang, J. S. Electron-hole diffusion lengths > 175 μm in solution-grown $CH_3NH_3PbI_3$ single crystals. *Science* **2015**, *347*, 967–970.

[11] Nie, W. Y.; Tsai, H.; Asadpour, R.; Blancon, J. C.; Neukirch, A. J.; Gupta, G.; Crochet, J. J.; Chhowalla, M.; Tretiak, S.; Alam, M. A. et al. High-efficiency solution-processed perovskite solar cells with millimeter-scale grains. *Science* **2015**, *347*, 522–525.

[12] Dong, H. Y.; Zhang, L. X.; Zhang, W. H.; Wang, J. L.; Zhang, X. L.; Ding, L. M. Single crystals of perovskites. *J. Semicond.* **2022**, *43*, 120201.

[13] Guo, Z.; Wan, Y.; Yang, M. J.; Snaider, J.; Zhu, K.; Huang, L. B. Long-range hot-carrier transport in hybrid perovskites visualized by ultrafast microscopy. *Science* **2017**, *356*, 59–62.

[14] Shi, D.; Adinolfi, V.; Comin, R.; Yuan, M. J.; Alarousu, E.; Buin, A.; Chen, Y.; Hoogland, S.; Rothenberger, A.; Katsiev, K. et al. Low trap-state density and long carrier diffusion in organolead trihalide perovskite single crystals. *Science* **2015**, *347*, 519–522.

[15] Lian, Z. P.; Yan, Q. F.; Gao, T. T.; Ding, J.; Lv, Q. R.; Ning, C. G.; Li, Q.; Sun, J. L. Perovskite $CH_3NH_3PbI_3$(Cl) single crystals: Rapid solution growth, unparalleled crystalline quality, and low trap density toward $10^8$ $cm^{-3}$. *J. Am. Chem. Soc.* **2016**, *138*, 9409–9412.

[16] Han, Q. F.; Bae, S. H.; Sun, P. Y.; Hsieh, Y. T.; Yang, Y.; Rim, Y. S.; Zhao, H. X.; Chen, Q.; Shi, W. Z.; Li, G. et al. Single crystal formamidinium lead iodide ($FAPbI_3$): Insight into the structural, optical, and electrical properties. *Adv. Mater.* **2016**, *28*, 2253–2258.

[17] Liu, Y. C.; Zhang, Y. X.; Yang, Z.; Feng, J. S.; Xu, Z.; Li, Q. X.; Hu, M. X.; Ye, H. C.; Zhang, X.; Liu, M. et al. Low-temperature-gradient crystallization for multi-inch high-quality perovskite single crystals for record performance photodetectors. *Mater. Today* **2019**, *22*, 67–75.

[18] Li, Y. L.; Ding, L. M. Single-crystal perovskite devices. *Sci. Bull.* **2021**, *66*, 214–218.

[19] Chen, Y. X.; Ge, Q. Q.; Shi, Y.; Liu, J.; Xue, D. J.; Ma, J. Y.; Ding, J.; Yang, H. J.; Hu, J. S.; Wan, L. J. General space-confined on-substrate fabrication of thickness-adjustable hybrid perovskite single-crystalline thin films. *J. Am. Chem. Soc.* **2016**, *138*, 16196–16199.

[20] Gu, Z. K.; Huang, Z. D.; Li, C.; Li, M. Z.; Song, Y. L. A general printing approach for scalable growth of perovskite single-crystal films. *Sci. Adv.* **2018**, *4*, eaat2390.

[21] Yang, Z. Q.; Deng, Y. H.; Zhang, X. W.; Wang, S.; Chen, H. Z.; Yang, S.; Khurgin, J.; Fang, N. X.; Zhang, X.; Ma, R. M. High-performance single-crystalline perovskite thin-film photodetector. *Adv. Mater.* **2018**, *30*, 1704333.

[22] Kelso, M. V.; Mahenderkar, N. K.; Chen, Q. Z.; Tubbesing, J. Z.; Switzer, J. A. Spin coating epitaxial films. *Science* **2019**, *364*, 166–169.

[23] Xiao, X.; Dai, J.; Fang, Y. J.; Zhao, J. J.; Zheng, X. P.; Tang, S.; Rudd, P. N.; Zeng, X. C.; Huang, J. S. Suppressed ion migration along the in-plane direction in layered perovskites. *ACS Energy Lett.* **2018**, *3*, 684–688.

[24] Peng, W.; Wang, L. F.; Murali, B.; Ho, K. T.; Bera, A.; Cho, N.; Kang, C. F.; Burlakov, V. M.; Pan, J.; Sinatra, L. et al. Solution-grown monocrystalline hybrid perovskite films for hole-transporter-free solar cells. *Adv. Mater.* **2016**, *28*, 3383–3390.

[25] Zhumekenov, A. A.; Burlakov, V. M.; Saidaminov, M. I.; Alofi, A.; Haque, A.; Turedi, B.; Davaasuren, B.; Dursun, I.; Cho, N.; El-Zohry, A. M. et al. The role of surface tension in the crystallization of metal halide perovskites. *ACS Energy Lett.* **2017**, *2*, 1782–1788.

[26] Wang, K.; Wu, C. C.; Yang, D.; Jiang, Y. Y.; Priya, S. Quasi-two-dimensional halide perovskite single crystal photodetector. *ACS Nano* **2018**, *12*, 4919–4929.

[27] Liu, Y.; Dong, Q. F.; Fang, Y. J.; Lin, Y. Z.; Deng, Y. H.; Huang, J. S. Fast growth of thin $MAPbI_3$ crystal wafers on aqueous solution surface for efficient lateral-structure perovskite solar cells. *Adv. Funct. Mater.* **2019**, *29*, 1807707.

[28] Malinkiewicz, O.; Yella, A.; Lee, Y. H.; Espallargas, G. M.; Graetzel, M.; Nazeeruddin, M. K.; Bolink, H. J. Perovskite solar cells employing organic charge-transport layers. *Nat. Photonics* **2014**, *8*, 128–132.

[29] Po, R.; Carbonera, C.; Bernardi, A.; Camaioni, N. The role of buffer layers in polymer solar cells. *Energy Environ. Sci.* **2011**, *4*, 285–310.

[30] Lei, Y. S.; Chen, Y. M.; Zhang, R. Q.; Li, Y. H.; Yan, Q. Z.; Lee, S.; Yu, Y. G.; Tsai, H.; Choi, W.; Wang, K. P. et al. A fabrication process for flexible single-crystal perovskite devices. *Nature* **2020**, *583*, 790–795.

[31] Rao, H. S.; Li, W. G.; Chen, B. X.; Kuang, D. B.; Su, C. Y. *In situ* growth of 120 $cm^2$ $CH_3NH_3PbBr_3$ perovskite crystal film on FTO glass for narrowband-photodetectors. *Adv. Mater.* **2017**, *29*, 1602639.

[32] Tang, X. B.; Chen, W.; Wu, D.; Gao, A. J.; Li, G. M.; Sun, J. Y.; Yi, K. Y.; Wang, Z. J.; Pang, G. T.; Yang, H. C. et al. *In situ* growth of all-inorganic perovskite single crystal arrays on electron transport layer. *Adv. Sci.* **2020**, *7*, 1902767.

[33] Zhao, L. Y.; Gao, Y.; Su, M.; Shang, Q. Y.; Liu, Z.; Li, Q.; Wei, Q.; Li, M. L.; Fu, L.; Zhong, Y. G. et al. Vapor-phase incommensurate heteroepitaxy of oriented single-crystal $CsPbBr_3$ on GaN: Toward integrated optoelectronic applications. *Acs Nano* **2019**, *13*, 10085–10094.

[34] Liu, Y. C.; Ren, X. D.; Zhang, J.; Yang, Z.; Yang, D.; Yu, F. Y.; Sun, J. K.; Zhao, C. M.; Yao, Z.; Wang, B. et al. 120 mm single-crystalline perovskite and wafers: Towards viable applications. *Sci. China Chem.* **2017**, *60*, 1367–1376.

[35] Wang, K.; Wu, C. C.; Hou, Y. C.; Yang, D.; Priya, S. Monocrystalline perovskite wafers/thin films for photovoltaic and transistor applications. *J. Mater. Chem. A* **2019**, *7*, 24661–24690.

[36] Chen, Y. M.; Lei, Y. S.; Li, Y. H.; Yu, Y. G.; Cai, J. Z.; Chiu, M. H.; Rao, R.; Gu, Y.; Wang, C. F.; Choi, W. et al. Strain engineering and epitaxial stabilization of halide perovskites. *Nature* **2020**, *577*, 209–215.

[37] Liu, Y. C.; Zhang, Y. X.; Yang, Z.; Ye, H. C.; Feng, J. S.; Xu, Z.; Zhang, X.; Munir, R.; Liu, J.; Zuo, P. et al. Multi-inch single-crystalline perovskite membrane for high-detectivity flexible photosensors. *Nat. Commun.* **2018**, *9*, 5302.

[38] Cheng, X.; Yang, S.; Cao, B. Q.; Tao, X. T.; Chen, Z. L. Single crystal perovskite solar cells: Development and perspectives. *Adv. Funct. Mater.* **2020**, *30*, 1905021.

[39] Li, L. Y.; Liu, J. X.; Zeng, M. Q.; Fu, L. Space-confined growth of metal halide perovskite crystal films. *Nano Res.* **2021**, *14*, 1609–1624.

[40] Dunlap-Shohl, W. A.; Zhou, Y. Y.; Padture, N. P.; Mitzi, D. B. Synthetic approaches for halide perovskite thin films. *Chem. Rev.* **2019**, *119*, 3193–3295.

[41] Tang, X. B.; Wang, Z. J.; Wu, D.; Wu, Z. H.; Ren, Z. W.; Li, R. X.; Liu, P.; Mei, G. D.; Sun, J. Y.; Yu, J. H. et al. *In situ* growth mechanism for high-quality hybrid perovskite single-crystal thin films with high area to thickness ratio: Looking for the sweet spot. *Adv. Sci.* **2022**, *9*, 2104788.

[42] Yao, F.; Peng, J. L.; Li, R. M.; Li, W. J.; Gui, P. B.; Li, B. R.; Liu, C.; Tao, C.; Lin, Q. Q.; Fang, G. J. Room-temperature liquid diffused separation induced crystallization for high-quality perovskite single crystals. *Nat. Commun.* **2020**, *11*, 1194.

[43] Ma, L.; Yan, Z. G.; Zhou, X. Y.; Pi, Y. Q.; Du, Y. P.; Huang, J.; Wang, K. W.; Wu, K.; Zhuang, C. Q.; Han, X. D. A polymer controlled nucleation route towards the generalized growth of organic-inorganic perovskite single crystals. *Nat. Commun.* **2021**, *12*, 2023.

[44] Wang, Z. J.; Shan, C. W.; Liu, C. X.; Tang, X. B.; Luo, D. F.; Tang, H. D.; Song, Z. L.; Wang, J. W.; Ren, Z. W.; Ma, J. R. et al. *In situ* growth of perovskite single-crystal thin films with low trap density. *Cell Rep. Phys. Sci.* **2023**, *4*, 101363.

[45] Tiller, W. A. *The Science of Crystallization: Microscopic Interfacial Phenomena*; Cambridge University Press: Cambridge, 1991.

[46] Hutter, E. M.; Muscarella, L. A.; Wittmann, F.; Versluis, J.; McGovern, L.; Bakker, H. J.; Woo, Y. W.; Jung, Y. K.; Walsh, A.; Ehrler, B. Thermodynamic stabilization of mixed-halide perovskites against phase segregation. *Cell Rep. Phys. Sci.* **2020**, *1*, 100120.

[47] Chen, Y. N.; He, M. H.; Peng, J. J.; Sun, Y.; Liang, Z. Q. Structure and growth control of organic-inorganic halide perovskites for optoelectronics: From polycrystalline films to single crystals. *Adv. Sci.* **2016**, *3*, 1500392.

[48] Nakada, K.; Matsumoto, Y.; Shimoi, Y.; Yamada, K.; Furukawa, Y. Temperature-dependent evolution of Raman spectra of methylammonium lead halide perovskites, $CH_3NH_3PbX_3$ (X = I, Br). *Molecules* **2019**, *24*, 626.

[49] Liu, Y. C.; Zhang, Y. X.; Zhu, X. J.; Feng, J. S.; Spanopoulos, I.; Ke, W. J.; He, Y. H.; Ren, X. D.; Yang, Z.; Xiao, F. W. et al. Triple-cation and mixed-halide perovskite single crystal for high-performance X-ray imaging. *Adv. Mater.* **2021**, *33*, 2006010.

[50] Guo, Y. L.; Sato, W.; Shoyama, K.; Halim, H.; Itabashi, Y.; Shang, R.; Nakamura, E. Citric acid modulated growth of oriented lead perovskite crystals for efficient solar cells. *J. Am. Chem. Soc.* **2017**, *139*, 9598–9604.

[51] Zhao, Y. X.; Zhu, K. Organic–inorganic hybrid lead halide perovskites for optoelectronic and electronic applications. *Chem. Soc. Rev.* **2016**, *45*, 655–689.

[52] Stoumpos, C. C.; Kanatzidis, M. G. The renaissance of halide perovskites and their evolution as emerging semiconductors. *Acc. Chem. Res.* **2015**, *48*, 2791–2802.

[53] Zhang, C. Y.; Wang, Y. B.; Lin, X. S.; Wu, T. H.; Han, Q. F.; Zhang, Y. Q.; Han, L. Y. Effects of a site doping on the crystallization of perovskite films. *J. Mater. Chem. A* **2021**, *9*, 1372–1394.

[54] Sun, Y. Q.; Mao, L.; Yang, T.; Zhang, H.; Shi, J. H.; Tan, Q. C.; Li, F. M.; Zeng, P.; Gong, J.; Liu, Z. X. et al. Ionic liquid modified polymer intermediate layer for improved charge extraction toward efficient and stable perovskite/silicon tandem solar cells. *Small* **2024**, *20*, 2308553.

[55] Tian, C. M.; Wu, T. H.; Zhao, Y.; Zhou, X. L.; Li, B.; Han, X. F.; Li, K. R.; Hou, C. Y.; Li, Y. G.; Wang, H. Z. et al. Anion-stabilized precursor inks toward efficient and reproducible air-processed perovskite solar cells. *Adv. Energy Mater.* **2024**, *14*, 2303666.

[56] Liu, Y. C.; Sun, J. K.; Yang, Z.; Yang, D.; Ren, X. D.; Xu, H.; Yang, Z. P.; Liu, S. Z. 20-mm-large single-crystalline formamidinium-perovskite wafer for mass production of integrated photodetectors. *Adv. Opt. Mater.* **2016**, *4*, 1829–1837.

[57] You, P.; Li, G. J.; Tang, G. Q.; Cao, J. P.; Yan, F. Ultrafast laser-annealing of perovskite films for efficient perovskite solar cells. *Energy Environ. Sci.* **2020**, *13*, 1187–1196.

[58] Guerrero, A.; Bisquert, J.; Garcia-Belmonte, G. Impedance spectroscopy of metal halide perovskite solar cells from the perspective of equivalent circuits. *Chem. Rev.* **2021**, *121*, 14430–14484.

[59] Wang, K.; Yang, D.; Wu, C. C.; Shapter, J.; Priya, S. Mono-crystalline perovskite photovoltaics toward ultrahigh efficiency. *Joule* **2019**, *3*, 311–316.

[60] Lei, Y. S.; Chen, Y. M.; Xu, S. Single-crystal halide perovskites: Opportunities and challenges. *Matter* **2021**, *4*, 2266–2308.

[61] Li, J. Y.; Han, Z. Y.; Gu, Y.; Yu, D. J.; Liu, J. X.; Hu, D. W.; Xu, X. B.; Zeng, H. B. Perovskite single crystals: Synthesis, optoelectronic properties, and application. *Adv. Funct. Mater.* **2021**, *31*, 2008684.

[62] Fang, Y. J.; Dong, Q. F.; Shao, Y. C.; Yuan, Y. B.; Huang, J. S. Highly narrowband perovskite single-crystal photodetectors enabled by surface-charge recombination. *Nat. Photonics* **2015**, *9*, 679–686.

[63] Lou, Y. J.; Zhang, S. S.; Gu, Z. K.; Wang, N.; Wang, S. H.; Zhang, Y. Q.; Song, Y. L. Perovskite single crystals: Dimensional control, optoelectronic properties, and applications. *Mater. Today* **2023**, *62*, 225–250.

[64] Kresse, G.; Hafner, J. *Ab initio* molecular dynamics for open-shell transition metals. *Phys. Rev. B* **1993**, *48*, 13115–13118.

[65] Kresse, G.; Furthmüller, J. Efficiency of *ab-initio* total energy calculations for metals and semiconductors using a plane-wave basis set. *Comput. Mater. Sci.* **1996**, *6*, 15–50.

[66] Kresse, G.; Furthmüller, J. Efficient iterative schemes for *ab initio* total-energy calculations using a plane-wave basis set. *Phys. Rev. B* **1996**, *54*, 11169–11186.

[67] Perdew, J. P.; Burke, K.; Ernzerhof, M. Generalized gradient approximation made simple. *Phys. Rev. Lett.* **1996**, *77*, 3865–3868.

[68] Blöchl, P. E. Projector augmented-wave method. *Phys. Rev. B* **1994**, *50*, 17953–17979.